Monthly Notices
of the
ROYAL ASTRONOMICAL SOCIETY

MNRAS **502,** 2023–2032 (2021)
Advance Access publication 2021 January 29

doi:10.1093/mnras/stab163

Flares in the Galactic Centre – I. Orbiting flux tubes in magnetically arrested black hole accretion discs

O. Porth ,[1]★ Y. Mizuno,[2,3] Z. Younsi[3,4] and C. M. Fromm[3,5,6,7]

[1]*Anton Pannekoek Institute for Astronomy, University of Amsterdam, Science Park 904, NL-1098 XH Amsterdam, the Netherlands*
[2]*Tsung-Dao Lee Institute, Shanghai Jiao Tong University, Shanghai 200240, China*
[3]*Institut für Theoretische Physik, Goethe Universität, Max-von-Laue-Straße 1, D-60438 Frankfurt am Main, Germany*
[4]*Mullard Space Science Laboratory, University College London, Holmbury St Mary, Dorking, Surrey RH5 6NT, UK*
[5]*Black Hole Initiative at Harvard University, 20 Garden Street, Cambridge, MA 02138, USA*
[6]*Center for Astrophysics – Harvard & Smithsonian, 60 Garden Street, Cambridge, MA 02138, USA*
[7]*Max-Planck-Institut für Radioastronomie, Auf dem Hügel 69, D-53121 Bonn, Germany*

Accepted 2021 January 16. Received 2020 December 11; in original form 2020 June 5

ABSTRACT

Recent observations of Sgr A∗ by the GRAVITY instrument have astrometrically tracked infrared (IR) flares at distances of ∼10 gravitational radii (r_g). In this paper, we study a model for the flares based on 3D general relativistic magnetohydrodynamic (GRMHD) simulations of magnetically arrested accretion discs (MADs) that exhibit violent episodes of flux escape from the black hole magnetosphere. These events are attractive for flare modelling for several reasons: (i) the magnetically dominant regions can resist being disrupted via magnetorotational turbulence and shear; (ii) the orientation of the magnetic field is predominantly vertical as suggested by the GRAVITY data; and (iii) the magnetic reconnection associated with the flux eruptions could yield a self-consistent means of particle heating/acceleration during the flare events. In this analysis, we track erupted flux bundles and provide distributions of sizes, energies, and plasma parameter. In our simulations, the orbits tend to circularize at a range of radii from ∼5 to 40 r_g. The magnetic energy contained within the flux bundles ranges up to $\sim 10^{40}$ erg, enough to power IR and X-ray flares. We find that the motion within the magnetically supported flow is substantially sub-Keplerian, in tension with the inferred period–radius relation of the three GRAVITY flares.

Key words: accretion, accretion discs – black hole physics – magnetic field – MHD – methods: numerical.

1 INTRODUCTION

Near-infrared (NIR) observations of the Galactic Centre have provided an exciting number of discoveries: foremost the precise measurement of the Galactic Centre black hole mass and distance of $M \simeq 4.15 \times 10^6$ and ≃8.178 kpc through astrometric monitoring of stellar orbits (Schödel et al. 2002; Ghez et al. 2003; Gravity Collaboration et al. 2019). Furthermore, the gravitational redshift and post-Newtonian orbit of S2 star were recently measured (Gravity Collaboration et al. 2018a, 2020a) setting tight bounds on the compactness of the central mass.

In addition to precision measurements of stellar orbits, NIR monitoring has revealed recurring ∼×10 flux increase flares that last for around an hour and occur roughly four times per day (Genzel et al. 2003). The peak intensity is $\sim 10^{35}$ erg s^{-1} and the emission is strongly polarized with changing polarization angle during the flare (Eckart et al. 2006; Trippe et al. 2007; Shahzamanian et al. 2015). Besides infrared (IR) flares, the Galactic Centre is also prone to simultaneous X-ray flares, albeit only one in four IR flares also has an X-ray counterpart (Baganoff et al. 2001; Porquet et al. 2003; Hornstein et al. 2007). The IR flares (but not the X-ray flares) exhibit substructure down to ∼1 min and large structural variations on time-scales of ∼20 min (Do et al. 2009; Dodds-Eden et al. 2009). These observations suggest a synchrotron origin of the IR emission from a compact region of size ∼3 r_g within ∼30 r_g from the black hole (Broderick & Loeb 2005; Witzel et al. 2018).

Recently, the Gravity Collaboration has reported three bright flares and astrometrically tracked their flux centroids with an accuracy of ∼2 r_g (Gravity Collaboration et al. 2018b, hereafter G18). The centroid positions and polarization swings with periods of 40–60 min were found to be compatible with a relativistic Keplerian circular orbit at 9 r_g (Gravity Collaboration et al. 2020b). A striking feature of these observations is that the polarization signature implies a strong poloidal component of the magnetic field in the emitting region (G18).

General relativistic magnetohydrodynamic (GRMHD) simulations of radiatively inefficient accretion are quite successful in reproducing many aspects of the galactic centre such as spectra, source sizes, and some aspects of variability and polarization signatures, yet no consensus model reproduces all observables at once (Mościbrodzka et al. 2009; Dexter et al. 2010; Dibi et al. 2012; Mościbrodzka & Falcke 2013; Chan et al. 2015a; Gold et al. 2017; Ressler et al. 2017; Chael et al. 2018; Anantua, Ressler & Quataert 2020). In the IR, large uncertainties are present due to the necessity of including electron heating and likely non-thermal processes in the radiative models (Chael, Narayan & Sadowski 2017; Chael et al. 2018; Davelaar et al. 2018).

★ E-mail: o.porth@uva.nl

Before exploring this large and uncertain parameter space, we here focus on the dynamics that could initiate IR flares like the ones observed by G18. In the context of the G18 flares, simulations of magnetically arrested discs (MAD; Igumenshchev, Narayan & Abramowicz 2003; Tchekhovskoy, Narayan & McKinney 2011; McKinney, Tchekhovskoy & Blandford 2012) are particularly promising. The simulations show frequent eruptions of excess magnetic flux from the saturated black hole magnetosphere. As first described by Igumenshchev (2008), these flux bundles appear as highly magnetized 'blobs' with a dominant poloidal magnetic field component in the accretion disc (e.g. Avara, McKinney & Reynolds 2016; Marshall, Avara & McKinney 2018; White, Stone & Quataert 2019). Once the excess flux is reaccreted, a repeating quasi-periodic cycle of outbursts from the black hole is set up.

The environment in which these eruptions occur is turbulent and complex and the mechanism behind the flux escape events is somewhat uncertain. Yet the process is reminiscent of a Rayleigh–Taylor-like interchange between funnel and disc plasma that is triggered once the accumulated magnetic pressure overcomes the ram pressure of the accretion stream (see e.g. the discussion in Marshall et al. 2018). Magnetic reconnection might be involved to promote accretion through the magnetic barrier (Igumenshchev et al. 2003) or to change topology of funnel field lines through a Y-point in the equatorial plane.

Large-scale simulations of mass feeding in the Galactic Centre through magnetized stellar winds have recently been presented by Ressler, Quataert & Stone (2019, 2020). They demonstrate that for a wide range of initial wind magnetizations, the (extrapolated) horizon scale magnetic field is of order of the MAD limit. Similar to MAD accretion, the inner magnetic field is dominated by the poloidal component and magnetorotational instability (MRI) is either marginally or fully suppressed. This serves as additional strong motivation to study MAD dynamics in context of Sgr A∗ flares.

This paper is organized as follows. In Section 2, we first describe the GRMHD simulations and analyse timing properties of various diagnostics in the simulations. We then elucidate on the flux eruption mechanism and describe our method of flux tube selection for the following statistical analysis. We conclude in Section 3.

2 RESULTS

2.1 Overall characteristics of the simulations

In this paper, we discuss GRMHD simulations obtained with BHAC(Porth et al. 2017; Olivares et al. 2019)[1] using modified Kerr–Schild coordinates (McKinney & Gammie 2004) and two to three levels of static mesh refinement. Unless stated explicitly, we use units where $G = c = 1$, which for instance sets the length unit $r_g = M$, where M is the mass of the black hole. The simulations are initialized with a hydrodynamic equilibrium torus following Fishbone & Moncrief (1976) with inner edge at $r_{in} = 20\,M$ and density maximum at $r_{max} = 40\,M$ and we use an ideal equation of state with an adiabatic index of $\hat{\gamma} = 4/3$. We perturb the initial state by adding a purely poloidal magnetic field capable of saturating the black hole flux. The particular vector potential reads

$$A_\phi \propto \max\left[\left(\frac{r_{KS}}{r_{in}}\right)^3 \sin\theta_{KS}\, \exp\left(-r_{KS}/400\right)\,(\rho - 0.01)\,,\, 0\right], \quad (1)$$

[1] https://www.bhac.science

Table 1. Overview of the simulations giving spin, resolution, mass-weighted average quality factors, and domain size.

ID	a	$N_r \times N_\theta \times N_\phi$	$\langle Q_r\rangle_\rho \times \langle Q_\theta\rangle_\rho \times \langle Q_\phi\rangle_\rho$	r_{out}
MAD-128	+0.9375	256 × 128 × 128	18.9 × 14.4 × 29.6	2500 M
MAD-192	+0.9375	384 × 192 × 192	27.2 × 22.4 × 43.0	2500 M
MAD-192-CR	−0.9375	384 × 192 × 192	25.0 × 21.2 × 31.3	2500 M
SANE-256	+0.9375	512 × 256 × 128	10.6 × 11.4 × 10.3	2110 M

where subscript KS indicates ordinary Kerr–Schild coordinates. The initial magnetic field is weak and scaled such that the ratio of pressure maxima $\beta_{ini} := p_{gas,\,max}/p_{mag,\,max}$ adopts a value of $\beta_{ini} = 100$.

An overview of the simulations used in this paper is given in Table 1. With the fiducial (dimensionless) spin value of $a = 0.9375$, we discuss two MAD cases with increasing resolutions and one standard and normal evolution (SANE) case for comparison. In addition, a counter-rotating case with $a = -0.9375$ is shown to investigate the spin dependence of the results. To check for convergence of the simulations, we also quote the mass-weighted MRI quality factors (Q-factors, see Section 2.3) in Table 1. As indicated by Q-factors above 10, all simulations have sufficient resolution to capture the MRI (e.g. Hawley, Guan & Krolik 2011; Sorathia et al. 2012; Hawley et al. 2013).

2.2 Time series

A time series of horizon penetrating fluxes following the definitions of Porth et al. (2019) is shown in Fig. 1. A quasi-stationary MAD state is obtained after $t = 7500\,M$, where the dimensionless horizon penetrating magnetic flux $\phi := \Phi_{BH}/\sqrt{|\dot{M}|}$ reaches the critical value of $\phi_{max} \approx 15$ for $a = +0.9375$ and $\phi_{max} \approx 8$ for $a = -0.9375$, consistent with Tchekhovskoy, McKinney & Narayan (2012).[2] Quasi-periodic dips in the horizon penetrating magnetic flux are visible in particular in the counter-rotating case where up to half of the flux is expelled in strong events. The flux is then reaccreted and the expulsion repeats after a time-scale of 1000–2000 M that corresponds to ∼5–10 h in the galactic centre. In the corotating case, we see weaker flux expulsions and correspondingly the time-scale of reaccretion is considerably shorter. The normalized accretion power measured at the event horizon, $|(\dot{E} - \dot{M})/\dot{M}|$, shows an efficiency of up to ∼150 per cent, indicating the extraction of spin energy and is a characteristic property of the MAD state (Tchekhovskoy et al. 2012).

Turning to the rotation profiles that are given through the power law:

$$\Omega(r) \propto r^{-q}, \quad (2)$$

with index q. While the SANE case is compatible with Keplerian motion ($q = 1.43$), once large flux tubes appear around $t \sim 12\,000\,M$, the MAD case becomes substantially sub-Keplerian ($q = 1.25$) due to additional magnetic support. The rotation and shear will be analysed further in Section 2.6.

It is interesting to consider how accretion of mass and magnetic flux are interrelated for MAD discs. Naively, if accretion proceeds through an interchange process, one might expect $\dot{M}(t)$ and $\dot{\Phi}_{BH}(t)$ to be anticorrelated. This is because dense plasma (increasing M) is 'interchanged' with strongly magnetized funnel plasma (decreasing Φ_{BH}). However, as pointed out also by Beckwith, Hawley & Krolik

[2] In our system of units, which differs from the commonly employed definition of Tchekhovskoy et al. (2011, 2012) and McKinney et al. (2012) by a factor of $\sqrt{4\pi}$.

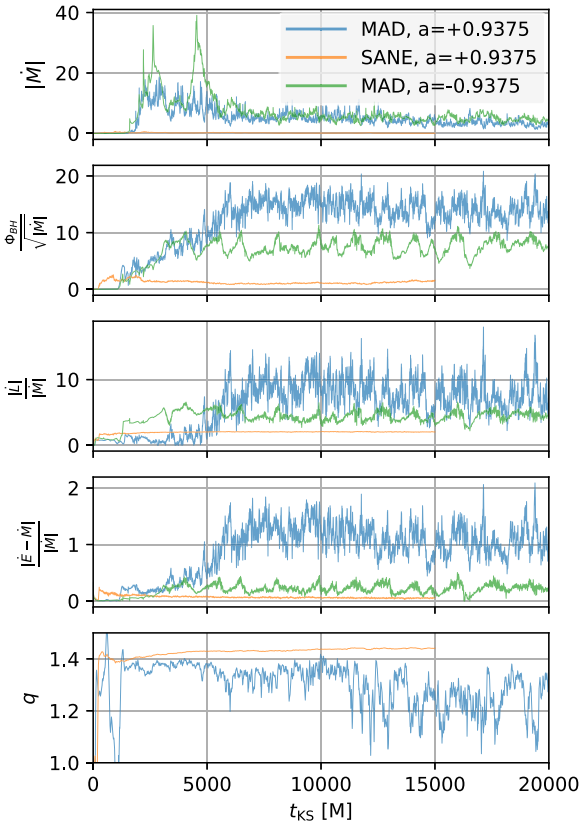

Figure 1. Time series of the MAD accretion runs (blue, green) contrasted with the SANE case (orange). Horizon-penetrating fluxes reach the MAD limits at $t_{KS} \simeq 7500\,M$. In the corotating case, the energy extraction is more than 100 per cent of the accretion power at this time. Large flux tubes appear at $t \sim 12\,000\,M$ that coincides with strong fluctuations in the rotation index q. Rotation in the SANE case on the other hand is only slightly sub-Keplerian with index of $q = 1.43$ within $t_{KS} \in [5000, 10\,000]\,M$. The rotation index has been omitted for the counter-rotating case at it is not well fitted by a power law.

(2009), the black hole mass *must* increase, whereas magnetic flux can also decrease due to 'escape' from the black hole and due to the accretion of opposite polarity field lines and reconnection. Hence it is not clear whether a correlation between the two properties should exist at all, as different processes might govern their respective evolutions.

To analyse the accretion process, as a first step, we investigate the autocorrelation of the rates of mass $\dot{M}$, energy and angular momentum $\dot{E}$ and $\dot{L}$, and the rate of magnetic flux increase $\dot{\Phi}_{BH}$. The correlation time is defined as the lag when the autocorrelation assumes a value of $1/e$ and the time series is restricted to a time when the simulations are firmly in the MAD state: $t \in [10\,000, 15\,000]\,M$. This yields a correlation time for the (detrended) $\dot{M}$ of $t_{corr,\dot{M}} = 47$ and $65\,M$ for the fiducial runs `MAD-128` and `MAD-192`, respectively. These values are consistent with the decorrelation time of the ray-traced synthetic images used in the Event Horizon Telescope (EHT) model fitting (Event Horizon Telescope Collaboration et al. 2019). Repeating this analysis for $\dot{E}$ and $\dot{L}$ yields similar results. Quite in contrast to $\dot{M}$, $\dot{E}$, and $\dot{L}$, it turns out that in our simulations $\dot{\Phi}_{BH}$ is uncorrelated down to the sampling frequency of $1\,M$, both for the MAD and SANE cases. Accordingly, there is no detectable correlation between mass accretion and $\dot{\Phi}$. This is a strong indication that the black hole flux in the saturated state is subject to a highly intermittent random process and does not follow the long-term trends seen in the accretion of mass.

We have further checked for cross-correlations between the aforementioned quantities and note one striking difference between the SANE and MAD cases: in turbulent SANE accretion, the time series of $\dot{M}$ and $\dot{L}$ is clearly anticorrelated, meaning low-density streams of gas carry higher than average specific angular momentum. The MAD cases show no clear correlation. A possible interpretation could be: if angular momentum of low-density flux tubes is removed via large-scale stresses in MAD accretion, it is expected that these low-density flux tubes carry systematically lower angular momentum when they are accreted. Hence one would expect a positive correlation between $\dot{M}$ and $\dot{L}$. If both turbulent MRI accretion and flux tube accretion occur at the same time, likely no correlation is observed.

2.3 Flux tube selection

Flux tubes are dominated by coherent large-scale vertical magnetic fields. They differ substantially from the MRI active regions where the field is subdominant and its geometry is mostly toroidal. This is visualized in Fig. 2, where we chose footpoints rooted on: the black hole event horizon (white field lines), in the MRI active turbulent disc (yellow lines), and in a high-magnetization region in the equatorial plane (red). Here we introduce the (hot) magnetization $\sigma := b^2/(\rho h)$ that compares the square of the fluid-frame field strength b^2 and the enthalpy density of the gas ρh. Within one scale height of the disc, the flux tube remains nearly vertical and is subsequently wound up around the jet. Its mid-plane magnetization is $\sigma \simeq 0.5$ and, as the field is strong, the MRI is quenched in the flux tube.

The suppression of the MRI is quantified by the 'MRI suppression factor' that compares the disc scale height H with the wavelength of the fastest growing (vertical) MRI mode $\lambda^{(\tilde{\theta})}$. No growth is expected for wavelengths that do not 'fit' into the disc diameter, hence for $S_{MRI} := {}^{2H}/_{\lambda^{(\tilde{\theta})}} < 1$. For a quantitative analysis, we define the density weighted averages as

$$\langle\,\cdot\,\rangle_\rho\,(r,\theta,t) := \frac{\int_0^{2\pi}(\,\cdot\,)\,\rho(r,\theta,\phi,t)\sqrt{-g}\,\mathrm{d}\phi}{\int_0^{2\pi}\rho(r,\theta,\phi,t)\sqrt{-g}\,\mathrm{d}\phi}, \tag{3}$$

$$\langle\,\cdot\,\rangle_\rho\,(r) := \frac{\int_{t_{beg}}^{t_{end}}\int_0^{2\pi}\int_0^{\pi}(\,\cdot\,)\,\rho(r,\theta,\phi,t)\sqrt{-g}\,\mathrm{d}\theta\,\mathrm{d}\phi\,\mathrm{d}t}{\int_{t_{beg}}^{t_{end}}\int_0^{2\pi}\int_0^{\pi}\rho(r,\theta,\phi,t)\sqrt{-g}\,\mathrm{d}\theta\,\mathrm{d}\phi\,\mathrm{d}t}, \tag{4}$$

with $(\,\cdot\,)$ denoting the quantity being averaged, g is the determinate of the four metrics, and where we set an averaging interval in the quasi-stationary state $t_{beg} = 12\,000\,M$ and $t_{end} = 15\,000\,M$. We measure the (density) scale height as

$${}^{H}/_{r}\,(r) := \langle\,|\pi/2 - \theta_{KS}|\,\rangle_\rho\,(r). \tag{5}$$

The fastest growing mode is evaluated in a comoving orthonormal reference frame (Takahashi 2008) as

$$\lambda^{(\theta)} := \frac{2\pi}{\Omega\sqrt{\rho h + b^2}}\,b^{(\theta)}, \tag{6}$$

where $\Omega := u^\phi/u^t$ is the coordinate angular velocity of the fluid. We define the average suppression factor as

$$\langle S_{MRI}\rangle_\rho\,(r,\theta,t) := \frac{H(r)\,\langle\Omega\rangle_\rho(r)}{\pi\,\langle b^{(\theta)}/\sqrt{\rho h + b^2}\rangle_\rho(r,\theta,t)}, \tag{7}$$

and the MRI quality factors as

$$Q^{(i)} := \frac{\lambda^{(i)}}{\Delta x^{(i)}}, \qquad i \in (r,\theta,\phi). \tag{8}$$

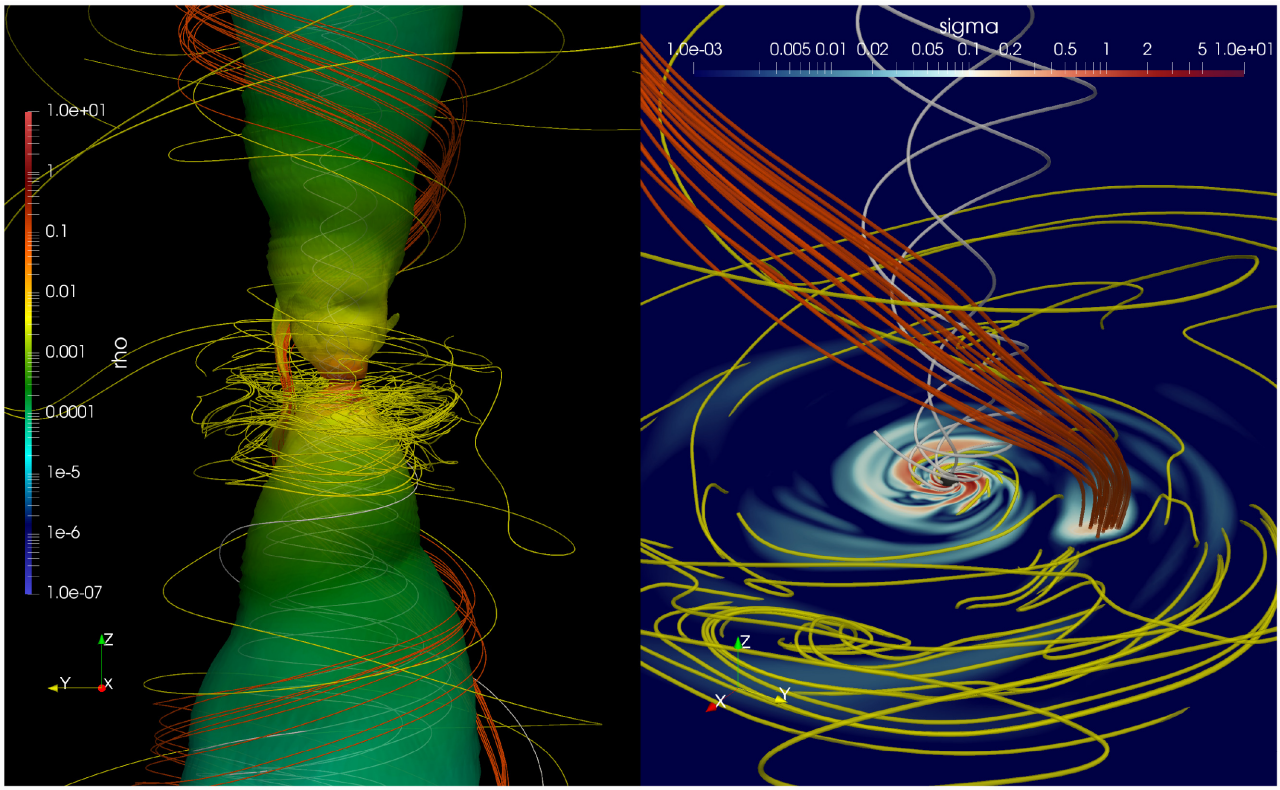

Figure 2. Rendering of the different magnetic field components in a MAD simulation. Horizon penetrating field lines (grey), toroidally dominated disc fields (yellow), and the expelled flux tube (red). In the left-hand panel, we show the isocontour $\sigma = 0.2$ coloured by density. In the right-hand panel, the mid-plane mangetization σ is indicated, highlighting also the magnetized flux tube.

The mass-weighted averages of the Q-factors within $r < 50\,M$ are noted for each run in Table 1.

Effectively, the suppression factor means that MRI does not grow in magnetically dominated regions. This can be seen using the thin disc relation $c_s = \Omega H$ and noting that $v_A^{(\theta)} = b^{(\theta)}/\sqrt{\rho h + b^2}$ is the vertical Alfvén velocity. Hence

$$S_{\rm MRI} \approx {}^{c_s}\!/_{v_A} \approx \sqrt{{}^{P_{\rm gas}}\!/_{B_z^2}}, \tag{9}$$

simply compares the sound and Alfvén velocities or magnetic and thermal pressure contributions.

To identify flux tubes for further analysis, we therefore look for regions with dominant vertical field component and trace the contours where $B_z^2/P_{\rm gas} = 1$ in the equatorial plane. In addition, to reduce the level of noise in the detection, we restrict our analysis to flux tubes with a cross-section of at least $1/(4\pi r_{\rm h}^2)$ in area, where $r_{\rm h}$ is the radius of the black hole event horizon. We have verified, using these criteria, that for the SANE case this comparison does not show any flux tubes.

Fig. 3 illustrates the properties of these regions for three consecutive times for simulation `MAD-128`. The flux tubes selected in this fashion have dominant out-of-plane magnetic fields that were checked by tracing their field lines as in Fig. 2 for several selected cases. Fig. 3 shows that flux tubes coincide with suppressed MRI (top panels), and have low plasma β and higher than average σ, as expected (bottom two rows). It is interesting to note that in both runs `MAD-128` and `MAD-192`, we find that the angle- and time-averaged $\langle S_{\rm MRI}\rangle_\rho\,(r)$ suggests MRI suppression within $\sim 10\,M$. However, within this radius, dense streams of accreting material are frequently found where the MRI can in principle operate.

2.4 Dynamics of flux tubes

Over time, a flux tube will become more elongated as it shears out in the differentially rotating accretion flow. Flux and mass conservation for constant scale height yields a simple estimate for the pressure contributions in the flux tube:

$$B_z^2 \propto \Delta r^{-4}, \tag{10}$$

$$P_{\rm gas} \propto \Delta r^{-2\hat{\gamma}}, \tag{11}$$

where Δr is a measure of the size of the flux tube (here defined as the radius of the circle having the same surface as the cross-sectional area of the flux tube). Hence for any causal $\hat{\gamma} < 2$, the magnetic pressure decreases faster than the thermal pressure as the flux tube increases in size. As the flux tube moves outwards, the ambient pressure decreases and pressure equilibrium is obtained via expansion of the tube, hence the flux tube expands and loses its magnetic dominance. Shear- and Rayleigh–Taylor-induced mixing can also increase the size of the flux tube over time. Once distributed over a large area, the flux tube cannot remain magnetically dominated and is dissipated in the accretion flow.

To analyse the motion of the flux tubes, we compute the centroid of the magnetic flux in the selected magnetically dominated regions in the equatorial plane, illustrated by '+' signs in Fig. 3. The centroid motions of robust features that can be tracked for at least one-quarter of a circle are illustrated in Fig. 4. A flux bundle spirals outwards to eventually circularize at what we call its 'circularization radius'. For different flux tubes we recover different circularization radii ranging up to $\sim 40\,M$. Over the considered time interval $t_{\rm KS} \in [12\,000,\ 15\,000]\,M$, the high-resolution `MAD-192` case shows

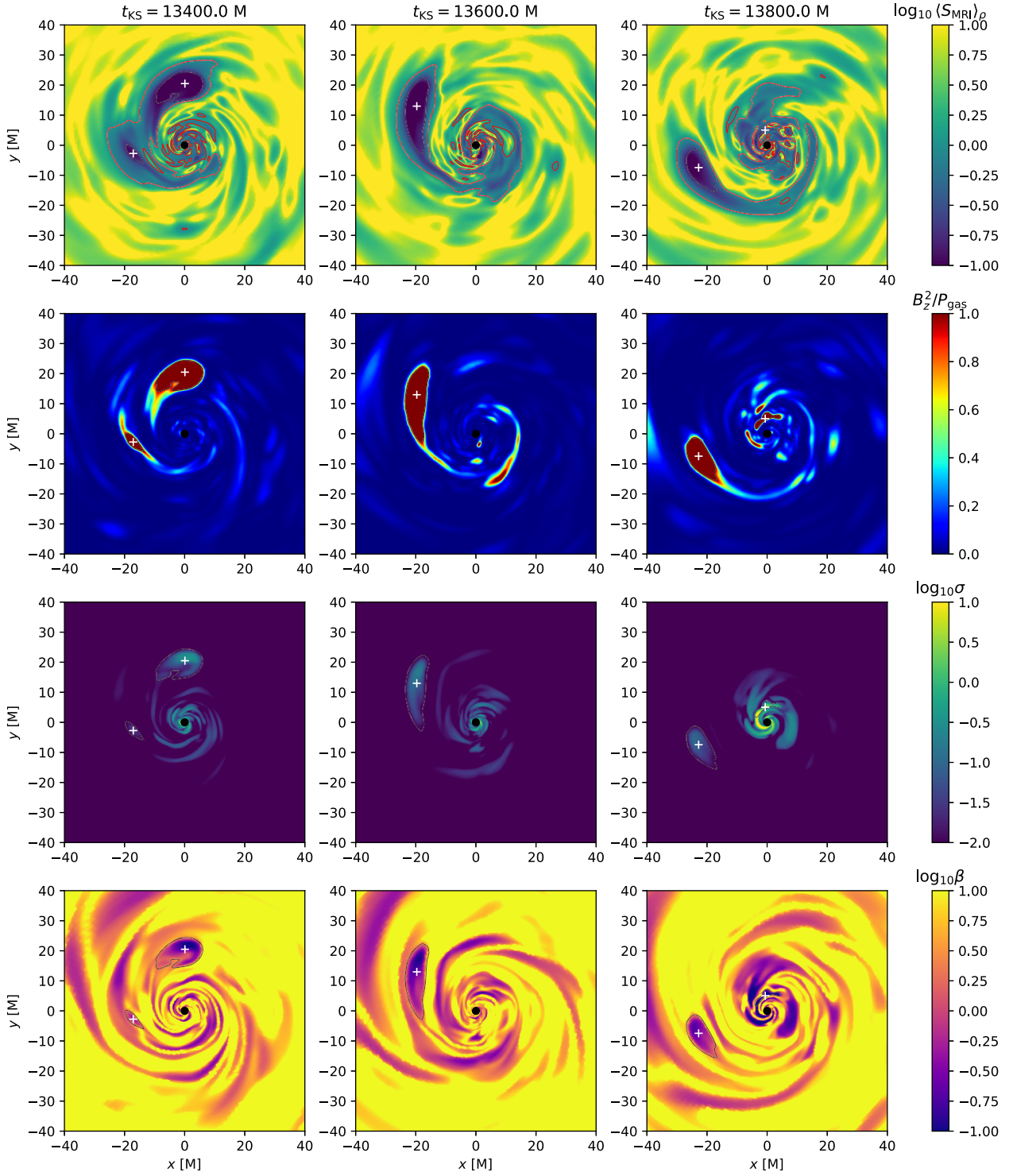

Figure 3. Evolution of quantities in the equatorial plane. We show the density-weighted MRI suppression factor $\langle S_{MRI}\rangle_\rho$ marking the region where MRI is suppressed by the red contour (top panels). The second row illustrates B_z^2/P_{gas} used for extraction of flux tubes on the equatorial plane. Magnetization and corresponding plasma β parameter are given in the third and fourth row. Flux tubes have a dominant vertical field energy B_z^2 compared to the gas pressure and suppress the MRI. At a radius of $\sim$20 M a large flux tube performs a circular orbit while shearing out in the differentially rotating flow. In the lower three panels, contours mark the detection threshold and crosses mark the flux centroid position.

fewer eruptions than MAD-128, yet the parameters of the present features are comparable.

Key parameters of the flux tube evolution are summarized in Fig. 5 where we show the coordinate values r, ϕ, the relative size of the magnetically dominated region, $\Delta r/r$, and the magnetic energy contained within one density scale height, E_B. To compute the normalization for the latter, we perform ray-tracing radiative transfer of the data using the BHOSS code (Younsi & Wu 2015)

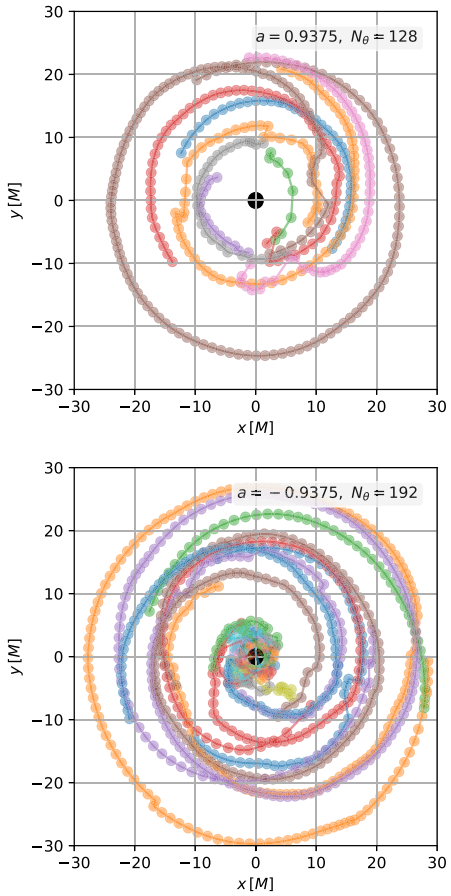

Figure 4. Flux centroids positions for the simulations `MAD-128` and `MAD-192-CR`. We only show data for flux bundles that can be traced for at least one-quarter orbit. The centroid positions spiral outwards and reach nearly circular orbits before the flux bundle dissolves. We recover a wide range of the circularization radii and the counter-rotating case also shows tracks in the direct vicinity of the black hole.

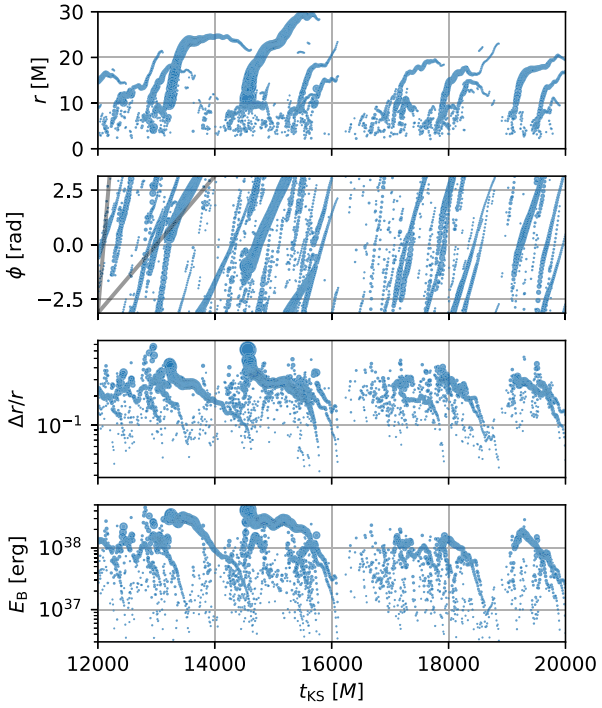

Figure 5. Time evolution of the orbiting flux tubes identified in simulation `MAD-128`. The first two panels represent the coordinates of the magnetic flux centroid in the equatorial plane. In the third panel, we show the relative size of the flux tube and the fourth panel shows the magnetic energy contained in the flux tube within one disc scale height. Symbols are scaled according magnetic flux and grey lines indicating orbital periods of 200 and 2000 M have been added in the third panel to guide the eye.

and scale the simulations to recover the Galactic Centre flux of $F_\nu \simeq 2.4\,\mathrm{Jy}$ observed at an EHT frequency of 230 GHz (Doeleman et al. 2008). We apply an inclination of 45° and 'standard parameters' from the M87 modelling (Event Horizon Telescope Collaboration et al. 2019): $R_{\rm high} = 10$ and adopt a high-σ cut-off $\sigma_{\rm cut} = 1$.

By tracing the radius and azimuth, it is seen that flux tubes generally move outwards from the black hole due to the magnetic tension of the highly pinched fields and slow down their radial motion to orbit at constant radius between ∼5 and 40 M. As flux tubes are eroded by the ambient flow and decrease in magnetization, just before they dissolve, the detected (radial) centroid motions become erratic. This is reflected in the first panel of Fig. 5 as seemingly inward or outward moving features observed after circularization. The large variance in circularization radii indicates that the final resting place of the flux bundles is not given by the magnetospheric radius (which on average lies ≃10). Rather, we find that when the field enters a circular orbit it has also adopted a predominantly vertical orientation and hence no tension force is available to drive it out further.

Orbital periods between 200 and 2000 M are recovered in our simulations, depending on the radial location of the fields. Because of the increase of plasma β (and thus decrease of the tracer quantity $B_z^2/P_{\rm gas}$), the inferred size and magnetic energy gradually decrease until the flux tube is no longer detected as a magnetically dominated region. At its maximum, the magnetic energy reaches $\sim 5 \times 10^{38}$ erg for both the `MAD-128` and `MAD-192` simulations.

2.5 Distributions

The instantaneous distributions of various flux tube properties are shown in Fig. 6. Small flux tubes with $\Delta r \sim 0.5$–$1\,M$ close to the detection cut-off dominate in number, but sizes of up to $7\,M$ are recovered. As shown in the top panel of Fig. 6, the range of magnetic energies spans over two orders of magnitude, from 3×10^{36} to 3×10^{38} erg in the corotating case and ranging up to 10^{40} erg in the counter-rotating case. The most probable magnetic energy of a flux tube is $\simeq 5 \times 10^{37}$ erg (corotating) and $\sim 10^{39}$ erg (counter-rotating), and large flux tubes are only found with high magnetic energies. However, smaller flux tubes are found at all magnetic energies.

Turning to the average plasma β and magnetization σ of the flux tubes, the distribution of plasma β peaks close to the detection threshold $\beta \simeq 2$ but extends down to ∼0.1. The magnetizations start at 0.01 with the peak at ∼0.1 and an extended tail ranging up to $\sigma = 10$. The counter-rotating case has a broader distribution of σ with a second peak at $\sigma \simeq 3$. Efficient particle acceleration via magnetic reconnection requires the plasma to be magnetically dominated, hence $\sigma > 1$ and $\beta < 1$. In our sample, we find that this is the case for ∼10 per cent of the identified features. We have carried out this analysis for both `MAD-128` and `MAD-192` runs, finding that

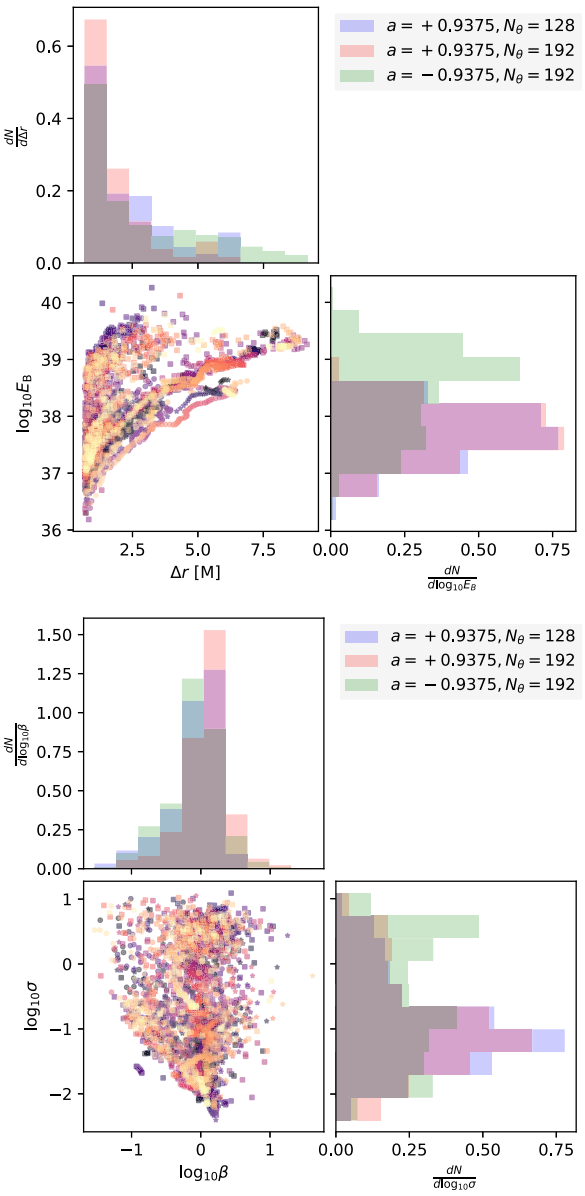

Figure 6. Distribution of the flux tubes identified in the MAD simulations. Most of the flux tubes have small radii $\lesssim 2\,M$ and magnetic energies of $\sim 10^{38}$ erg for the corotating case and $\sim 10^{39}$ erg for the counter-rotating case. Typically, β is of order unity and magnetizations $\sigma \sim 0.1$, although also highly magnetized cases $\sigma \in [1, 10]$ are observed in particular in the counter-rotating case that shows a much broader distribution.

these results are quite insensitive to the choice of resolution and run.

2.6 Shearing analysis

As in any differentially rotating flow, azimuthally advected features are destined to wind up and lose their coherence. Naturally, while magnetically dominated and subject to large-scale tension force, flux bundles are not readily sheared however. In some sense, they behave more like the spoon that stirs the tea rather than the milk in it. Over time however, they will lose magnetic dominance (see Section 2.4) and it is instructive to consider how long such 'passive tracers' can remain coherent in a given differential rotation profile. This should

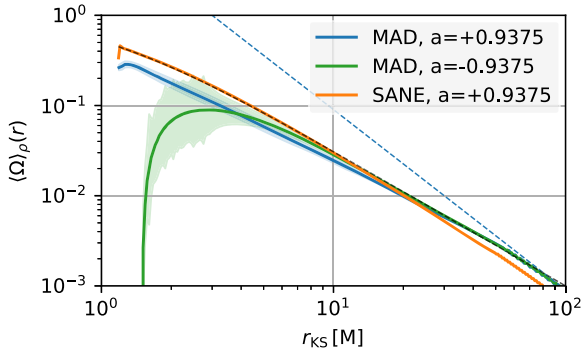

Figure 7. Disc and time-averaged rotation profiles in the SANE and MAD runs for an averaging interval of $t \in [12\,000,\ 15\,000]\,M$. The dashed blue curve indicates the rotation law of the initial data $q = 2$ and the dashed black curve a relativistic Keplerian profile. The inner regions of the SANE run are consistent with Keplerian rotation. Shaded areas underlying the curves denote the standard deviation of the profiles in time (only visible in the MAD cases).

provide a lower limit to the survival of the flux tubes against shear. Given a rotation law of the form (2), for a feature contained within $[r, r + \Delta r]$, the inner edge will 'lap' the slower moving outer component after one shearing time-scale:

$$t_{\rm shear} := P(r)\left[\frac{1}{1-(1+\Delta r/r)^{-q}}\right].$$

We show the rotation profile of the simulations $\langle\Omega\rangle_\rho(r)$ in Fig. 7. In the SANE case, the rotation in the inner quasi-stationary regions is described by a relativistic Keplerian motion $\Omega_{\rm K} := 1/(a + r^{3/2})$ (dashed black curve) that is fitted by a power law for $r \in [2, 20]\,M$ with $q = 1.44$. Because of additional magnetic support, the inner regions of the corotating MAD case are sub-Keplerian with a shallower power-law index of $q \simeq 1.25$. In the counter-rotating case, large departures from Keplerian motion are observed within the innermost stable circular orbit (ISCO) of $\sim 9\,M$ and the violent ejection of large flux bundles reflects the large variance of the rotation profile within $\sim 5\,M$.

Varying q in the range [1.25, 1.5], however, does not significantly alter the shearing time-scale. This means that small features with $\Delta r/r < 0.1$ can in principle survive for ~ 10 orbital periods, whereas large features with $\Delta r/r \sim 1$ would be smeared out after roughly one orbit. For the majority of the detected features with relative sizes $\Delta r/r \in [0.1, 0.3]$, differential rotation allows several orbits before the features would be fully smeared out due to shear.

2.7 Orbital periods

The three astrometrically tracked flares from 2018 reported by G18 have shown motion on scales of $\sim 10\,M$. Although only one orbit appears closed, within the measurement errors, all three flares can be explained by a single Keplerian circular orbit with a radius of $9\,M$ (Gravity Collaboration et al. 2020b). While not statistically significant, Gravity Collaboration et al. (2020b) note that the sizes of the flux centroid motions appear to be systematically larger than the model predictions. In other words, the model Keplerian motion at the observed centroid position is too slow compared to the observational data. Recently, Matsumoto, Chan & Piran (2020) analysed the July 22 flare with a broader range of models including marginally bound geodesics and super-Keplerian pattern motion, confirming this finding. They also find that a super-Keplerian circular orbit with $\Omega = 2.7\Omega_{\rm K}$ at $r = 12.5\,M$ yields a better match to the data

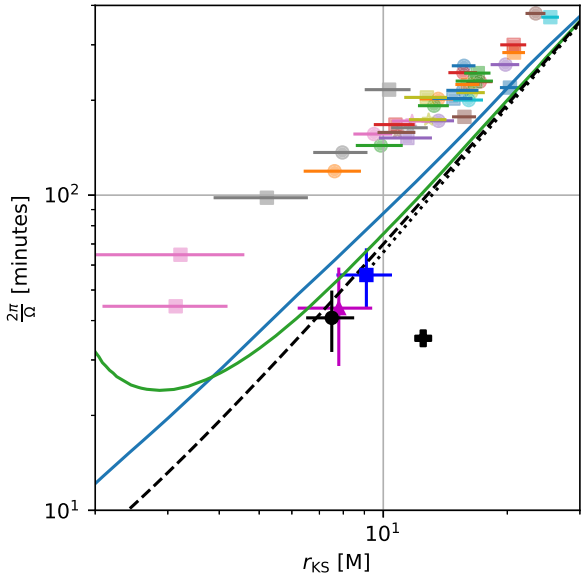

Figure 8. Periods against average radius for the features where at least half an orbit can be tracked. All data are scaled to Sgr A∗. Star symbols refer to run `MAD-192`, discs to `MAD-128`, and squares to `MAD-192-CR`. Blue and green curves show the periods based on $\langle\Omega\rangle_\rho(r)$ (cf. Fig. 7) and dashed (dotted) curve the expected Keplerian profiles for prograde (retrograde) spin. We also reproduce the data points from the analysis of G18 (blue, magenta, and black points). The black '+' symbol is the super-Keplerian fit to the 2018 July 22 flare from Matsumoto et al. (2020). Generally, the orbital periods are sub-Keplerian and even somewhat slower than the density-weighted average rotation profile.

than the Keplerian orbits. However, as the measurement errors are substantial, all models are formally acceptable at present.

With the features found in the GRMHD simulations, it is interesting to ask how their orbital periods compare to the data of the flares. To this end, we need to track features over time in the simulation data. Our algorithm works as follows: (1) with a cadence of $10\,M$, we obtain the boundary curves of the magnetically dominated flux tubes in the equatorial plane as described in Section 2.3; (2) for two consecutive snapshots, we identify a flux tube from the second snapshot with a previously identified flux tube from the first snapshot when their surfaces S_1 and S_2 contained within the two boundary curves overlap by at least 20 per cent. This overlap is formally computed as the surface of the intersection between S_1 and S_2 normalized to their union: $S_1 \cap S_2 / S_1 \cup S_2$.

We verify that this leads to a robust tracking by visually inspecting several test cases. Fig. 8 shows the (mean) orbital periods against radius for all features that can be traced for at least 180°. To illustrate the radial evolution, we show the standard deviation of the radial coordinate as an error bar. As comparison cases, we also overplot (i) the data points from G18 that have been modelled as Keplerian orbits, and (ii) the 'super-Keplerian' pattern motion fit from Matsumoto et al. (2020).

As shown by the figure, all features are significantly sub-Keplerian and are also slower than the average local rotation velocity by a factor of typically ∼2. The counter-rotating case shows an abundance of features in the inner region. These are much slower (up to ∼5 times) than the average flow and exhibit strong radial variation as flux tubes are expelled with large outward velocities. Hence the fastest feature we could observe has an orbital period of ∼40 min. Inspecting the instantaneous coordinate velocities of the tracked features, apart from a handful of outliers due to small uncertainties in tracking, here we also do not find any evidence for super-Keplerian motion in the centroid motions. Therefore, as MAD flows have generically sub-Keplerian rotation profiles (Igumenshchev et al. 2003) and flux tubes tend to 'lag behind' even further due to the magnetic torques exerted by them (Spruit & Uzdensky 2005; Igumenshchev 2008), the MAD model is in tension with the apparent observed fast rotations (respectively large radii of the centroids).

3 DISCUSSION AND CONCLUSIONS

In MAD discs, low-density, high-magnetization flux bundles are frequently expelled from the black hole magnetosphere. As a candidate scenario for the astrometrically resolved flares observed by G18, we have analysed the dynamics and energetics of these magnetized regions.

Since the flux bundles coincide with regions of suppressed MRI turbulence, they can remain coherent in the accretion flow for several orbital time-scales. For the features identified in our simulations, orbital shear would set an upper limit of 1–10 orbits, depending on the size that varies from $\Delta r/r \simeq 0.1$ to 1. In practice, a maximum of roughly two orbits was observed before features ceased to be detected as magnetically dominated regions in the accretion flow. As strongly magnetized flux tubes are stabilized by the magnetic tension, orbital shear cannot solely be responsible for the destruction of flux bundles however.

Driven outward by magnetic tension from the radially pinched fields, flux bundles initially move out radially and then follow circular orbits when the field has straightened out to an essentially vertical structure. The model can therefore explain orbiting features at a range of radii. We propose that the dissolution of the flux bundle is governed by the following two effects: as the outward moving flux bundle seeks pressure equilibrium with its surroundings, it is forced to expand that leads to a decrease of its magnetic dominance. Differential rotation and local-shear-induced Kelvin–Helmholtz instabilities (e.g. Antolin, Yokoyama & Van Doorsselaere 2014; White et al. 2019) are then available to erode the surface of the flux bundle.

By running one counter-rotating case with spin $a = -0.9375$, we have checked that the flux bundles orbiting at relevant radial distances of $\sim 10\,M$ do not depend significantly on black hole spin. Differences arise mainly within $r = 2$–$3\,M$, where the counter-rotating case exhibits a steeply declining rotation profile. However, in the counter-rotating case, the flux bundles are more energetic by an order of magnitude. This results from two effects: first, the lower radiative efficiency of the counter-rotating case implies that for the same normalizing mm-flux, a higher accretion rate and density are required. Second, the eruptions found in the counter-rotating case remove a larger fraction of magnetic flux from the black hole (up to ∼50 per cent) resulting in stronger flares.

We have computed distributions of sizes, magnetization, and energy contained within the flux bundles for the corotating and counter-rotating cases. When the simulations are scaled to match the 230 GHz flux of the Galactic Centre, we find that the most probable magnetic energy in the corotating case is $\sim 5 \times 10^{37}$ erg and $\sim 10^{39}$ erg in the counter-rotating case. The latter distribution however extends all the way up to $\sim 10^{40}$ erg. Given that strong flares radiate up to 10^{38} erg in X-rays (Baganoff et al. 2001; Hornstein et al. 2007; Bouffard et al. 2019), the counter-rotating case has sufficient magnetic energy to allow for a radiative efficiency of a few per cent. In our sample, in ∼10 per cent of the cases, we found average plasma parameters with $\sigma > 1$ and $\beta < 1$, allowing for efficient particle acceleration via magnetic reconnection.

While magnetic reconnection likely plays a role in the expulsion of magnetic flux from the black hole, due to the highly variable nature of the inner dynamics, it is difficult to identify clear signatures of a

topology change of the magnetic field. Two-dimensional (resistive) GRMHD simulations of MAD discs by Ripperda, Bacchini & Philippov (2020) on the other hand have shown an episodically forming equatorial current sheet endowed with a plasmoid chain – a smoking gun of reconnection. It is an intriguing possibility that flux threading the black hole might escape via reconnecting through this equatorial current sheet as it can provide a means of loading the flux bundles with relativistic particles. In our simulations, azimuthal interchange instabilities do not allow a strong current sheet to persist and the flow is continuously perturbed by spiral stream of accreting material. The mechanism that we envision was recently also described in the context of protostellar flares by Takasao et al. (2019). In their resistive MHD simulations, reconnection in the equatorial region heats plasma associated with flux removal from the star leading to flare energies consistent with X-ray observations. Future resistive 3D GRMHD simulations will be better suited to elucidate the nature of magnetic reconnection in MAD accretion as it enables a parametric exploration of the resistivity.

An important constraint for the flaring model comes from the period–radius relation of the flares. Whereas the observations by G18 suggest Keplerian or even super-Keplerian motion (Matsumoto et al. 2020), since MAD discs are sub-Keplerian and flux bundles tend to lag by an additional factor of $\sim$2 in the periods (as already pointed out by Igumenshchev 2008), there is some tension with the current observations. In this regard, it is important to consider alternative models like the ejected plasmoids studied by Younsi & Wu (2015), Ball et al. (2020), and Nathanail et al. (2020). In this model, the emission originates from outward moving plasmoids that form due to magnetic reconnection in the coronal regions of the accretion flow. The changed geometry can yield an explanation for the offset between the mean centroid position and the black hole (Ball et al. 2020) and reconcile the super-Keplerian motion due to finite light-traveltime effects (Gravity Collaboration et al. 2020b). Whether the model can also explain the energetics, polarization, and recurrence time of Sgr A$*$ flares remains to be seen.

It might be worthwhile to briefly entertain the possibility of a 'confusion scenario' to explain the apparent super-Keplerian nature of the 2018 July 22 flare: as multiple flux tubes can be present at the same time, one might wonder what are the chances that several independent flares in fact led to the observed characteristics. Our reasoning against it is as follows: if one were to observe multiple flaring tubes (not connected by some 'pattern motion signal'), it is quite unlikely that nine out of the 10 data points presented in G18 for the July 22 flare are monotonously increasing their azimuthal angle by a similar amount.[3] Of course one can argue whether truly nine confused flares are required to explain the data or whether one could do with less. None the less, we believe the odds are strongly stacked against the confusion scenario, even more so since as G18 note, 'all three flares can in principle be accounted by the same orbit model'.

It is necessary to discuss several caveats of our analysis. To detect flux bundles, we look for regions of suppressed MRI and identify features via the ratio of $B_z^2/P_{\rm gas} = 1$ in the equatorial plane. Changing the detection threshold can lead to more or less detected features altering slightly the quantitative distributions measured in Section 2.5. This has little influence, however, on the inferred motion of the magnetic flux centroid that is used for analysis of orbital periods carried out in Section 2.7.

In particular for MAD simulations, which show strong magnetizations and steep gradients of plasma parameters within the disc, it is important to check the resolution dependence of the results (White et al. 2019). To this end, we have carried out two simulations of the fiducial case, differing by a factor of 1.5 in resolution. We find that the results of our quantifications are generally consistent with each other and have combined both simulations to increase the available statistics of the analysis. It is so far unknown what sets the strength of the flux eruptions. Most likely, thin discs will experience stronger flares (Marshall et al. 2018), however a dependence on the initial conditions, e.g. the initial flux distribution in the disc, cannot yet be ruled out.

For a direct comparison with the observational data, one needs to compute the NIR intensity and polarization following a ray tracing through the simulation data. This is carried out in a recent parallel effort by Dexter et al. (2020) who use a long MAD simulation lasting for $6 \times 10^4\,M$ and apply (thermal) electron heating from (subgrid) magnetic reconnection models due to Werner et al. (2018). As the density in the escaping flux bundles is set by the funnel floors, emission of the flux bundles themselves is strongly suppressed. To estimate the emission from the flux bundles in our study, we have carried out the following experiment with the fiducial run: we apply a threshold $B_z^2/P_{\rm gas} \geq 10$ to only selected regions of strong vertical flux in the emitting volume. Applying the standard thermal emission model as described in Section 2.4, in particular $\sigma_{\rm cut} = 1$, we obtain a contribution of $\sim$0.5 per cent to the 230 GHz emission and the contribution to the 138 THz flux is even smaller $\sim 10^{-4}$. Raising the high-magnetization threshold to $\sigma_{\rm cut} = 25$ and again normalizing the accretion rate to recover the observed 230 GHz flux increases the total IR emission by a factor of $\sim$6 (from 0.006 ± 0.002 to 0.033 ± 0.01 Jy). For comparison: the equivalent increase found by Dexter et al. (2020) was a factor of $\sim$2. This increase is explained only to a very small part by the added contribution of disc-orbiting flux bundles (which have a median $\sigma \simeq 0.1$, e.g. Fig. 6) but is largely due to the strongly magnetized plasma near the jet wall. In fact, the strong dependence of the IR emission on $\sigma_{\rm cut}$ in MAD simulations is a known issue that was studied in detail within two-temperature simulations by Chael, Narayan & Johnson (2019) and our results are consistent with their findings. Hence any radiation modelling of IR emission has to deal to a smaller or larger degree with the arbitrary truncation via $\sigma_{\rm cut}$.

As discussed by Dexter et al. (2020), when the IR emission originates from disc plasma (using $\sigma_{\rm cut} = 1$), the emission at the boundary of the flux bundles is enhanced due to increased heating. Flux bundles thus stir up the accretion flow and their motion should also govern the IR centroid on the observational plane. The model of Dexter et al. (2020) shares many features with the observed flares that raise the hope that IR flares might be explained without invoking high-magnetization material that – in simulations – is plagued by arbitrary floor values and uncertain electron thermodynamics.

None the less, the radiative modelling is still complicated by the fact that at least for strong simultaneous X-ray and IR flares, additional physics of non-thermal particle acceleration is required (Markoff et al. 2001; Dodds-Eden et al. 2009; Chan et al. 2015b; Ball et al. 2016). Purely thermal models of IR flares relying on gravitational lensing events have also been proposed (Dexter & Fragile 2013; Chan et al. 2015b), but have difficulty in explaining the required flare amplitude and NIR spectral index. In fact, spectral

[3]Grossly and brazenly simplifying (and dropping the first data point that breaks the monotonous trend): if nine flux tubes are present at the same time and anyone can light up at any given time, only nine out of the nine! realizations would yield the observed ordering. This one in 40 320 chance does not even include yet the minute likelihood that nine independent large flares are observed within 30 min given the average flare rate (following Poissonian statistics) of around 4 $\rm d^{-1}$.

modelling indicates that a non-thermal tail in the distribution function is required both in quiescence and during the flare (Davelaar et al. 2018; Petersen & Gammie 2020). In particular the flat to inverted spectral index $\nu L_\nu \propto \nu^\alpha$ with $\alpha > 0$ during flares (Gillessen et al. 2006) is difficult to explain without invoking non-thermal particle acceleration. The 'redness' of the spectra produced by thermal distributions was also noted by Dexter et al. (2020) who included reconnection particle heating yet no non-thermal contributions. One scenario that comes to mind is that flux bundles can be loaded with relativistic electrons as they violently reconnect in the equatorial region just before a flux escape event. While this one-off acceleration mechanism might encounter problems explaining X-ray emission from synchrotron electrons that require continuous injection, a telltale signature of such an event would be the outward motion of the flux centroid at the onset of the flare, before it circularizes.

We plan to investigate the IR radiative signatures, foremost the flux centroid motion and polarization, incorporating various electron heating and acceleration prescriptions in a follow-up publication.

ACKNOWLEDGEMENTS

The authors thank the anonymous referee for raising several interesting points to enhance the discussion of this paper. YM and CMF are supported by the ERC synergy grant BlackHoleCam: Imaging the Event Horizon of Black Holes (grant number 610058). CMF is supported by the Black Hole Initiative at Harvard University, which is supported by a grant from the John Templeton Foundation. ZY is supported by a Leverhulme Trust Early Career Fellowship. The simulations were performed on GOETHE at the CSC-Frankfurt and Iboga at ITP Frankfurt. This research has made use of NASA's Astrophysics Data System (ADS).

DATA AVAILABILITY

The data underlying this paper will be shared on reasonable request to the corresponding author.

REFERENCES

Anantua R., Ressler S., Quataert E., 2020, MNRAS, 493, 1404
Antolin P., Yokoyama T., Van Doorsselaere T., 2014, ApJ, 787, L22
Avara M. J., McKinney J. C., Reynolds C. S., 2016, MNRAS, 462, 636
Baganoff F. K. et al., 2001, Nature, 413, 45
Ball D., Özel F., Psaltis D., Chan C.-k., 2016, ApJ, 826, 77
Ball D., Özel F., Christian P., Chan C.-K., Psaltis D., 2020, preprint (arXiv: 2005.14251)
Beckwith K., Hawley J. F., Krolik J. H., 2009, ApJ, 707, 428
Bouffard É., Haggard D., Nowak M. A., Neilsen J., Markoff S., Baganoff F. K., 2019, ApJ, 884, 148
Broderick A. E., Loeb A., 2005, MNRAS, 363, 353
Chael A. A., Narayan R., Sadowski A., 2017, MNRAS, 470, 2367
Chael A., Rowan M., Narayan R., Johnson M., Sironi L., 2018, MNRAS, 478, 5209
Chael A., Narayan R., Johnson M. D., 2019, MNRAS, 486, 2873
Chan C.-K., Psaltis D., Özel F., Narayan R., Saḍowski A., 2015a, ApJ, 799, 1
Chan C.-k., Psaltis D., Özel F., Medeiros L., Marrone D., Saḍowski A., Narayan R., 2015b, ApJ, 812, 103
Davelaar J., Mościbrodzka M., Bronzwaer T., Falcke H., 2018, A&A, 612, A34
Dexter J., Fragile P. C., 2013, MNRAS, 432, 2252
Dexter J., Agol E., Fragile P. C., McKinney J. C., 2010, ApJ, 717, 1092
Dexter J. et al., 2020, MNRAS, 497, 4999
Dibi S., Drappeau S., Fragile P. C., Markoff S., Dexter J., 2012, MNRAS, 426, 1928
Do T., Ghez A. M., Morris M. R., Yelda S., Meyer L., Lu J. R., Hornstein S. D., Matthews K., 2009, ApJ, 691, 1021
Dodds-Eden K. et al., 2009, ApJ, 698, 676
Doeleman S. S. et al., 2008, Nature, 455, 78
Eckart A., Schödel R., Meyer L., Trippe S., Ott T., Genzel R., 2006, A&A, 455, 1
Event Horizon Telescope Collaboration et al., 2019, ApJ, 875, L5
Fishbone L. G., Moncrief V., 1976, ApJ, 207, 962
Genzel R., Schödel R., Ott T., Eckart A., Alexander T., Lacombe F., Rouan D., Aschenbach B., 2003, Nature, 425, 934
Ghez A. M. et al., 2003, ApJ, 586, L127
Gillessen S. et al., 2006, J. Phys.: Conf. Ser., 54, 411
Gold R., McKinney J. C., Johnson M. D., Doeleman S. S., 2017, ApJ, 837, 180
Gravity Collaboration et al., 2018a, A&A, 615, L15
Gravity Collaboration et al., 2018b, A&A, 618, L10 (G18)
Gravity Collaboration et al., 2019, A&A, 625, L10
Gravity Collaboration et al., 2020a, A&A, 636, L5
Gravity Collaboration et al., 2020b, A&A, 635, A143
Hawley J. F., Guan X., Krolik J. H., 2011, ApJ, 738, 84
Hawley J. F., Richers S. A., Guan X., Krolik J. H., 2013, ApJ, 772, 102
Hornstein S. D., Matthews K., Ghez A. M., Lu J. R., Morris M., Becklin E. E., Rafelski M., Baganoff F. K., 2007, ApJ, 667, 900
Igumenshchev I. V., 2008, ApJ, 677, 317
Igumenshchev I. V., Narayan R., Abramowicz M. A., 2003, ApJ, 592, 1042
McKinney J. C., Gammie C. F., 2004, ApJ, 611, 977
McKinney J. C., Tchekhovskoy A., Blandford R. D., 2012, MNRAS, 423, 3083
Markoff S., Falcke H., Yuan F., Biermann P. L., 2001, A&A, 379, L13
Marshall M. D., Avara M. J., McKinney J. C., 2018, MNRAS, 478, 1837
Matsumoto T., Chan C.-H., Piran T., 2020, MNRAS, 497, 2385
Mościbrodzka M., Falcke H., 2013, A&A, 559, L3
Mościbrodzka M., Gammie C. F., Dolence J. C., Shiokawa H., Leung P. K., 2009, ApJ, 706, 497
Nathanail A., Fromm C. M., Porth O., Olivares H., Younsi Z., Mizuno Y., Rezzolla L., 2020, MNRAS, 495, 1549
Olivares H., Porth O., Davelaar J., Most E. R., Fromm C. M., Mizuno Y., Younsi Z., Rezzolla L., 2019, A&A, 629, A61
Petersen E., Gammie C., 2020, MNRAS, 494, 5923
Porquet D., Predehl P., Aschenbach B., Grosso N., Goldwurm A., Goldoni P., Warwick R. S., Decourchelle A., 2003, A&A, 407, L17
Porth O., Olivares H., Mizuno Y., Younsi Z., Rezzolla L., Moscibrodzka M., Falcke H., Kramer M., 2017, Comput. Astrophys. Cosmol., 4, 1
Porth O. et al., 2019, ApJS, 243, 26
Ressler S. M., Tchekhovskoy A., Quataert E., Gammie C. F., 2017, MNRAS, 467, 3604
Ressler S. M., Quataert E., Stone J. M., 2019, MNRAS, 482, L123
Ressler S. M., Quataert E., Stone J. M., 2020, MNRAS, 492, 3272
Ripperda B., Bacchini F., Philippov A. A., 2020, ApJ, 900, 100
Schödel R. et al., 2002, Nature, 419, 694
Shahzamanian B. et al., 2015, A&A, 576, A20
Sorathia K. A., Reynolds C. S., Stone J. M., Beckwith K., 2012, ApJ, 749, 189
Spruit H. C., Uzdensky D. A., 2005, ApJ, 629, 960
Takahashi R., 2008, MNRAS, 383, 1155
Takasao S., Tomida K., Iwasaki K., Suzuki T. K., 2019, ApJ, 878, L10
Tchekhovskoy A., Narayan R., McKinney J. C., 2011, MNRAS, 418, L79
Tchekhovskoy A., McKinney J. C., Narayan R., 2012, J. Phys.: Conf. Ser., 372, 012040
Trippe S., Paumard T., Ott T., Gillessen S., Eisenhauer F., Martins F., Genzel R., 2007, MNRAS, 375, 764
Werner G. R., Uzdensky D. A., Begelman M. C., Cerutti B., Nalewajko K., 2018, MNRAS, 473, 4840
White C. J., Stone J. M., Quataert E., 2019, ApJ, 874, 168
Witzel G. et al., 2018, ApJ, 863, 15
Younsi Z., Wu K., 2015, MNRAS, 454, 3283

This paper has been typeset from a TEX/LATEX file prepared by the author.